

Cite this: *Nanoscale*, 2016, 8, 4134

C₆₀ fullerene localization and membrane interactions in RAW 264.7 immortalized mouse macrophages†

K. A. Russ,^a P. Elvati,^b T. L. Parsonage,^{c,d} A. Dews,^a J. A. Jarvis,^{c,d} M. Ray,^a
B. Schneider,^a P. J. S. Smith,^{c,d} P. T. F. Williamson,^{c,d} A. Violi^{b,e} and M. A. Philbert^{*a}

There continues to be a significant increase in the number and complexity of hydrophobic nanomaterials that are engineered for a variety of commercial purposes making human exposure a significant health concern. This study uses a combination of biophysical, biochemical and computational methods to probe potential mechanisms for uptake of C₆₀ nanoparticles into various compartments of living immune cells. Cultures of RAW 264.7 immortalized murine macrophage were used as a canonical model of immune-competent cells that are likely to provide the first line of defense following inhalation. Modes of entry studied were endocytosis/pinocytosis and passive permeation of cellular membranes. The evidence suggests marginal uptake of C₆₀ clusters is achieved through endocytosis/pinocytosis, and that passive diffusion into membranes provides a significant source of biologically-available nanomaterial. Computational modeling of both a single molecule and a small cluster of fullerenes predicts that low concentrations of fullerenes enter the membrane individually and produce limited perturbation; however, at higher concentrations the clusters in the membrane causes deformation of the membrane. These findings are bolstered by nuclear magnetic resonance (NMR) of model membranes that reveal deformation of the cell membrane upon exposure to high concentrations of fullerenes. The atomistic and NMR models fail to explain escape of the particle out of biological membranes, but are limited to idealized systems that do not completely recapitulate the complexity of cell membranes. The surprising contribution of passive modes of cellular entry provides new avenues for toxicological research that go beyond the pharmacological inhibition of bulk transport systems such as pinocytosis.

Received 9th October 2015,
Accepted 21st January 2016

DOI: 10.1039/c5nr07003a

www.rsc.org/nanoscale

Introduction

Increasingly, nanomaterials such as C₆₀ fullerenes are incorporated into a wide variety of consumer products including sporting goods and batteries and are under review by the U.S. Food and Drug Administration and other agencies for approval in a broad array of drugs, medical devices, and consumer products. In comparison to bulk material of the same chemical composition, the inherent larger surface area per volume and

sub-cellular size of nanomaterials provide the significant potential for unanticipated and potentially adverse interactions with biological components.^{1,2}

Icosahedral in shape and with molecular diameter of approximately 1 nm, C₆₀ fullerenes are aromatic structures with π -orbital electrons that are readily donated for radical scavenging at biological pH,^{1,3} and are known to interact with cells. For example, the chemical attachment of drugs such as Paclitaxel and Doxorubicin to C₆₀ fullerenes has under experimental conditions improved pharmacokinetics and putatively enhanced therapeutic properties.⁴ Similarly, Doxorubicin bound to fullerenes displays increased solubility when compared to the drug alone.⁵

Aside from the potential for occupational exposures, fullerenes are produced by a wide array of naturally occurring events such as volcanic eruptions and wildfires and are produced by anthropogenic sources that employ low-temperature combustion of fossil fuels. Release of fullerenes into the atmosphere may result in widespread exposure to humans through the inhalation route.⁶ Due to their small aerodynamic radii these

^aToxicology Program, School of Public Health, University of Michigan, Ann Arbor, MI, USA. E-mail: philbert@umich.edu

^bMechanical Engineering, University of Michigan, Ann Arbor, MI, USA

^cCentre for Biological Science, University of Southampton, Highfield Campus, SO17 1BEJ Northern Ireland, UK

^dInstitute for Life Sciences, University of Southampton, Highfield Campus, SO17 1BJ Northern Ireland, UK

^eChemical Engineering, Biomedical Engineering, Biophysics, University of Michigan, Ann Arbor, MI, USA

†Electronic supplementary information (ESI) available. See DOI: 10.1039/c5nr07003a



particles gain access to the alveolar space and resident macrophages on the airway surface. Nanomaterials with an effective aerodynamic radius of 0.1–1 μm are sufficiently small to cross the alveolar epithelium and enter the adjacent bloodstream and circulating monocytes. Larger clusters of nanomaterial (>1 μm) exit the lung *via* the mucociliary escalator and may travel from the esophagus to the gut, through which they encounter the enteric immune system.⁷

Therefore, a greater understanding of interactions between nanomaterials and the various components of the innate immune system will enable the creation of better predictive models of adverse outcomes following exposure. As the barrier between the intracellular and extracellular compartments, the lipid membrane is an important structural component of cells. Investigations into the mechanisms by which nanomaterials interact with the lipid membrane, however, are challenging. Essentially every aspect of the nanomaterial, particularly composition and surface chemistry, affects the way it interacts with the lipid membrane. Size, shape, charge, presence of functional groups on the structure, protein corona formation, and ability to interact with receptors on the cellular surface for endocytosis are factors that determine the entry mechanism and rate of entry of the nanomaterials into the cell.⁸

Current research into the behavior of nanomaterials in biological systems, especially within the lipid membrane, has been limited by the ability to identify and track the nano-sized aggregates with currently available imaging technology. Due to the extremely small scale of the material and the complexity of living systems, in this paper we report on a three-pronged approach to determine the cellular distribution of C_{60} fullerenes with a particular focus on their interaction with the lipid membrane. *In vitro* experiments in RAW 264.7 immortalized mouse macrophages *via* biochemical/cytochemical techniques and biophysical measurements of model membranes *via* NMR are cross-referenced with computational models of nano-lipid interactions.

Methods

Physical characterization of pristine and functionalized fullerenes

Pristine fullerenes have very low solubility in water (<10^{−9} mg L^{−1}) and in the past they have, with some controversy, been dissolved in solvents such as tetrahydrofuran (THF) or have been replaced by functionalized fullerenes.⁹ Solvents are not an ideal vehicle for fullerenes due to their inherent toxic potential.¹⁰ Functionalization of fullerenes with hydroxyl groups or polyethylene glycol, for example, increases solubility but alters the way the nanomaterial interacts with biological systems.^{5,9} In this study fullerenes were prepared *via* the method of Deguchi *et al.*¹¹ and Spohn *et al.*¹² Specifically, this study combined the solvent exchange method with centrifugal filtration, which has been shown to remove major by-products tetrahydro-2-furanol, γ -butyrolactone, and peroxides identified in samples prepared in THF by solvent exchange.^{12,13} This two-

step method yielded the advantage of producing pristine or Tb@C_{60} fullerenes in water, without the contamination of THF byproducts that may unnecessarily produce skew the results of biological studies by the formation of chemically-induced radical species.

Full characterization of the Tb@C_{60} was performed and results were compared with pristine C_{60} fullerenes to confirm that the Tb@C_{60} is a proper substitute. We did this comparison with two separate methods: a Malvern Zetasizer was used to determine zeta potential and aggregate size; a Nanosight LM 14C was used to determine and compare the aggregate size of terbium particles and fullerenes. C_{60} fullerenes prepared on three separate days were analyzed for charge and aggregate size on each instrument.

Cell culture

RAW 264.7 immortalized mouse macrophages were obtained from American Type Culture Collection. They were maintained in Dulbecco's Modified Eagle Medium with 10% fetal bovine serum and 1% penicillin–streptomycin–glutamate solution. The cells were grown at 37 °C and 5% CO_2 . Cells were utilized until passage 30. Cell culture used both pristine fullerenes and terbium endohedral fullerenes.

Transmission electron microscope imaging

In order to obtain an initial perspective of the interaction between C_{60} fullerenes and lipids in RAW 264.7 immortalized mouse macrophages, TEM studies were utilized. RAW 264.7 cells were allowed to attach to the culture dish overnight. Subsequently, cells were dosed with 0.1 and 0.36 $\mu\text{g mL}^{-1}$ terbium-endohedral C_{60} fullerenes for 8 hours. They were fixed at 8 hours with glutaraldehyde and sodium phosphate buffer and refrigerated overnight. We took one precautionary step to preclude a likely procedural mishap. Specifically, cell pellets were not post-fixed with osmium tetroxide or counterstained with lead-citrate or uranyl-acetate to prevent the artifact of heavy metal nanometer-sized precipitates. Instead, cell pellets were dehydrated in graded alcohols, cleared, and embedded with epoxy resin for cutting of ultra-thin sections (about 45 nm thickness) in preparation for viewing on a Philips CM-100 transmission electron microscope. (This work was facilitated by the University of Michigan Microscopy and Image Analysis Team.) After the RAW 264.7 cells were dosed and processed as mentioned above. Size-distribution and morphology of C_{60} clusters was achieved by suspending terbium-endohedral C_{60} in water, drying on a TEM grid, and imaging on a Phillips CM-100 TEM.

Inhibition of endocytosis

The role of pinocytosis, endocytosis and phagocytosis in the cellular uptake of C_{60} was investigated using classical pharmacologic inhibitors (200 μM genistein for 30 minutes, 10 $\mu\text{g mL}^{-1}$ chlorpromazine hydrochloride (HCL), or 5 $\mu\text{g mL}^{-1}$ cytochalasin A).^{14–16}

Fullerene suspensions were added at a concentration of 4 $\mu\text{g mL}^{-1}$ and incubated for 3 hours. Cells were fixed with 4%



paraformaldehyde and stained with DAPI and antibodies against fullerenes and clathrin. The fullerene antibody was conjugated to Dylight 594. The clathrin secondary antibody was conjugated directly to FITC. Wide-field microscopy was performed with an Olympus IX-81 Disk Scanning Biological Microscope Imager, with an RGB plugin to quantify the amount of fullerene aggregates in the images. Fullerene aggregates were counted in four images of each inhibitor and four images of control cells exposed to only fullerenes. In each image, seven cells were assessed and the mean amount of red pixels in the images was calculated. Antibodies for C₆₀ were obtained from Santa Cruz Biotechnology, Inc., Dallas TX.

Freeze fracture

To visualize the fullerenes within the lipid membrane, we employed freeze-fracture TEM. RAW 264.7 cells were allowed to attach to culture flasks overnight. Cells were dosed with 0.5 $\mu\text{g mL}^{-1}$ terbium-endohedral fullerenes for 8 hours. They were fixed with glutaraldehyde and shipped to NanoAnalytical Laboratory for TEM imaging.

Preparation of vesicles containing C₆₀

A lipid precursor was manipulated and exposed to fullerenes as follows: 10 mg of d₃₁-POPC (Avanti Polar Lipids, US) were dissolved in 1 mL of chloroform/methanol (1 : 1), dried under a stream of nitrogen gas to form a thin lipid film, and then left under high vacuum overnight to remove trace amounts of solvent. The samples were rehydrated with either 30 μL double distilled water, 30 μL of 10.09 $\mu\text{g mL}^{-1}$ of C₆₀ in water, or 300 μL of 10.09 $\mu\text{g mL}^{-1}$ of C₆₀ in water. All samples were then subjected to five freeze/thaw cycles interspersed with vortexing. The samples were then lyophilized overnight, and then rehydrated with 30 μL of double distilled water and subjected to another five freeze/thaw cycles interspersed with vortexing. The samples were then transferred to a 4 mm, magic-angle spinning rotor for solid-state NMR studies.

Nuclear magnetic resonance spectroscopy

All NMR studies were conducted on a Chemagetics Infinity 400 MHz spectrometer equipped with a 4 mm, double-resonance, magic-angle spinning probe head. The sample temperature was calibrated using a methanol standard as previously described.¹⁷ Static ³¹P NMR spectra were recorded at 161.1 MHz using a Hahn-Echo pulse sequence with $\pi/2$ and π pulses of 5 μs and 10 μs duration, respectively, and an inter-pulse delay of 40 μs . During the echo and acquisition, 60 kHz continuous-wave proton decoupling was applied. Typically 1024 scans were acquired for each spectrum. Static ²H NMR spectra were recorded at 61 MHz using a quadrupolar echo sequence with $\pi/2$ pulses of 5 μs and an inter-pulse delay of 50 s. Typically 8192 scans were acquired for each spectrum. The ³¹P and ²H spectra were referenced to 85% H₃PO₄ and D₂O, respectively. All data processing was performed in matNMR.¹⁸ Prior to Fast Fourier Transform, ³¹P and ²H free induction decays left shifted to the top of the echo with 75 Hz and 250 Hz line broadening added, respectively.

The spectra were Depaked using a weighted Fast Fourier Transform algorithm¹⁹ and custom-written routines in Matlab (Mathworks Inc.). The observed quadrupolar splitting's (ν_Q^i) were used to calculate the order parameters (S_{CD}^i) directly:^{20–22}

$$S_{\text{CD}}^i = \frac{4}{3} \cdot \frac{\Delta\nu_Q}{\Delta\nu_Q^{\text{Static}}}$$

where ν_Q^{Static} is the static quadrupolar coupling constant (e^2qQ/h), which is 167 kHz for a paraffinic C–D bond.²³ The order parameter profiles were constructed based on previously published assignments.²⁴ Indeed, to quantify changes along the length of the acyl chains, we constructed order parameter profiles whereby the mobility of a given CD₂ group as characterized by the order parameter, S_{CD} , is plotted as a function of its position along the lipid chain.²⁵

Moment analysis was performed using a custom-written routine in Matlab (Mathworks Inc.). The n th moment is calculated as:

$$M_n = \frac{\int_0^\infty \omega^n S(\omega) d\omega}{\int_0^\infty S(\omega) d\omega}$$

where ω is the frequency and $S(\omega)$ is the signal intensity at a given frequency.²⁶

Molecular dynamics simulations

The NAMD software²⁷ was used to perform MD simulations together with the PLUMED plugin²⁸ for free-energy reconstructions. Atomic interactions were modeled by using CHARMM force field: CHARMM36²⁹ for the lipids, CGenFF³⁰ for fullerenes, and TIP3P³¹ for water. A time step of 2 femtoseconds (fs) was used to integrate all the forces except for columbic interactions, which were computed every 4 fs with the particle mesh Ewald method³² by using cubic functions on a 0.1 nm grid with a tolerance of 10^{-6} . A cutoff of 1.2 nm was employed for intermolecular forces and the potential was smoothed from 1 nm to the cutoff distance using the X-PLOR³³ 40 switching function, to avoid truncation effects. All the hydrogen bonds were kept rigid during the simulations with the SHAKE³⁴ algorithm.

A temperature of 310 K was maintained *via* a Langevin thermostat with a 20 ps^{−1} dumping coefficient, while the pressure of 1.01325 bar was imposed with the Nosé–Hoover Langevin piston method^{35,36} with a time constant of 100 fs for the pressure and 50 fs for the barostat temperature. Since the systems are inherently anisotropic, during production runs the dimension of the periodic box normal to the bilayer was allowed to vary independently from the other two axes (NPST ensemble).

Free-energy landscapes were reconstructed by employing the well-tempered Metadynamics algorithm.³⁷ Gaussians with an initial height of 0.3 kcal mol^{−1} were deposited every 0.5 ps, and bias factors between 20 and 35 were used depending on the system.

The initial configuration of lipid bilayers was produced with CharmmGUI³⁸ and then equilibrated for 20–40 ns with a



mix of NVT and NPsT simulations. In order to place the C_{60} cluster in the membrane, a cavity was gradually created in the center of the bilayer. After the cluster was inserted in the cavity, the system was equilibrated again.

Results and discussion

Regardless of the route of administration, nanomaterials entering the body will interact with cells of the innate immune system. The innate immune system is a nonspecific defense system that uses its component cells (macrophages, dendritic cells, neutrophils, mast cells, and natural killer) to identify, neutralize and dispose of particulate matter that may infect or otherwise damage the various internal compartments of the body. By contrast, the adaptive immune system uses a series of receptors that recognize specific antigens to recognize known threats such as microbial and other particulate stressors.³⁹ Nanomaterials that enter the body *via* the airway or blood will by virtue of diffusion (*e.g.*, the surface of the lung or in the vascular system) most commonly interact with macrophages in the alveoli or bloodstream. If recognized as foreign by the macrophage, uptake of the nanomaterial by the cell will depend on its physicochemical characteristics such as size, shape, surface charge, and surface functionalization. In general, larger nanoparticles or nanoparticles with a surface charge are more quickly recognized as foreign in comparison to smaller nanoparticles or neutral nanoparticles, respectively.⁴⁰ In addition to the original composition of the nanomaterial, protein interactions with relatively large (>50 nm hydrodynamic radius) clusters or agglomerates of the nanomaterial that result in stable adsorption of a protein corona alter interactions with the innate immune system. Such larger agglomerates may more freely interact with plasma proteins such as fibrinogen and albumin, further increasing overall size, altering surface charge, reactivity (*i.e.*, passivation of chemical surface of the nanomaterial while ‘opsonizing’ the surface making it biologically recognizable by cell surface receptors), and composition of the agglomerate. Such alteration of the nanomaterial surface may therefore confer on the nanomaterial those biological traits that allow interaction with cell surface receptors.⁴¹ If the nanomaterial is recognized as foreign, the macrophage will engulf and attempt to degrade the foreign material using a battery of oxidizing strategies that are effective against the usual microbiological threats to the body.³⁹ However, relatively little is known about the fate and transport of smaller agglomerates or individual nanoparticles (<50 nm hydrodynamic diameter) that are unable to have meaningful biochemical/physical interaction with macromolecules and are, themselves, sufficiently hydrophobic to enter the cell.

For this multifaceted study, we employed both pristine C_{60} fullerenes and functionalized fullerenes, of which the latter are required for imaging, particularly transmission electron microscope (TEM). For the functionalized fullerenes, we chose terbium-endohedral fullerenes $Tb@C_{60}$ since these

compounds contain terbium in their core, resulting in an electron-dense spot in the TEM images. We characterized the $Tb@C_{60}$ nanoparticles with comparison to pristine C_{60} fullerenes by determining zeta potential and aggregate size. The mean surface charge (zeta potential) of the C_{60} fullerene was -44.3 mV, and the $Tb@C_{60}$'s was -64.3 mV. The first value is in line with previous observations,^{42,43} while the endohedral fullerene shows an increased propensity to accumulate a negative charge. The most likely explanations for these findings are related to the comparatively big electron cloud surrounding the Tb atom, which has a radius between 0.177 and 0.1 nm (depending on the oxidation state and the definition used). Our analysis does not allow for a clear description of the phenomenon, which may for example be caused by a preferential aggregation of anions on the $Tb@C_{60}$ surface or by charge transfer (both inter- and intramolecular). However, we don't expect that the increased average negative charge would reflect in a markedly distinct behavior when it comes to interactions with cells or aggregation, as in both cases the values indicate a similarly stable dispersion of nanoparticles. A confirmation of this assumption comes from the comparable size of the aggregates, as measured by the Malvern Zetasizer: C_{60} and $Tb@C_{60}$ aggregates had an average hydrodynamic diameter of 91.13 and 99.31 nm, respectively (see Fig. S1 of the ESI†). The Nanosight LM 14C indicated an average hydrodynamic radius of 55.179 ± 34.16 nm (standard deviation) and 63.765 ± 24.46 nm, respectively (Fig. 1). The results show slight differences in measurements by the two instruments. This difference can be attributed to the tendency of the Zetasizer to skew towards larger aggregates. Regardless, the size determinations as well as the zeta potential determination suggest that the aggregates are similar; therefore, $Tb@C_{60}$ is a reasonable substitution for C_{60} fullerenes for the purpose of imaging.

To determine the uptake and localization of fullerenes, we exposed RAW 264.7 immortalized macrophages to $Tb@C_{60}$.

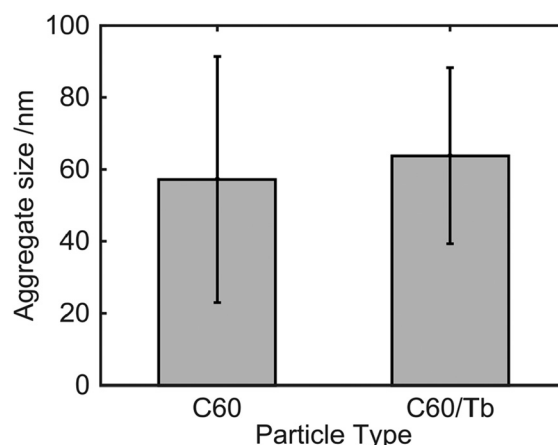


Fig. 1 Characterization of C_{60} fullerenes and terbium-endohedral fullerenes. Nanosight analysis of C_{60} fullerenes and $Tb@C_{60}$ aggregate size: C_{60} fullerene aggregates were approximately 55.179 nm with a standard deviation of 34.16 nm. $Tb@C_{60}$ aggregates were approximately 63.765 nm with a standard deviation of 24.46 nm.



This cellular exposure, at two different concentrations ($0.1 \mu\text{g mL}^{-1}$ and $0.36 \mu\text{g mL}^{-1}$ of C_{60}), was followed by TEM analysis of Tb@C_{60} distribution. Medium power electron microscope images of fixed cells in the absence of lead citrate and uranium acetate stains (which themselves deposit nanometer scale, electron dense crystals) do not provide compelling evidence that bulk transport of C_{60} nanoparticles is effected through phagocytosis or macropinocytosis (Fig. 2). However, several Tb-enhanced clusters of C_{60} are readily observed either without membranous investment in the cytosol (Fig. 2B), in close proximity to, or apparently integrated into cell and nuclear membranes (Fig. 2B and C). Analysis of epifluorescent images taken from cells preincubated with C_{60} and detected with a monoclonal antibody raised against pristine C_{60} enabled detection of cytoplasmic clusters of nanomaterial. Pharmacologic inhibition of endocytosis and macropinocytosis further confirmed minimal involvement of these membrane-mediated mechanisms of cellular uptake (Fig. 3). However, spectral analysis of images shows the entry of C_{60} clusters into the cytoplasm by other mechanisms. While it is possible that individual particles ($<1 \text{ nm}$ hydrodynamic diameter) could plausibly pass through channels or pores, it is unlikely that the larger clusters or agglomerates (as large as 80 nm) could take advantage of this pathway. The limitations of epifluorescent microscopy and spectroscopy permit acquisition of signal emitted from both large and small aggregates of C_{60} . However, the main focus of this manuscript is individual, and small clusters of C_{60} in the range $<5 \text{ nm}$: a size that has been postulated to account for the largest fraction of particles in most preparations of commercially available nanomaterial.⁴⁴ By contrast, caveolae are estimated to be about 50 nm in diameter^{45,46} and induce membrane invaginations with a minimal radius of curvature $\geq 90 \text{ nm}$.⁴⁷ Therefore, it is widely accepted that (at least for caveolin), materials need to be about 100 nm in diameter to trigger this important transport mechanism.

To further elucidate the observed interaction between the lipids of the cellular membrane and the fullerenes, freeze-fracture TEM was applied to cells dosed with Tb@C_{60} to visualize the fullerenes within the lipid membrane. Results are reported in the ESI, Fig. S2.† The fullerenes from the extracellular side appear to be entering the cytosol. We see aggregates of fullerenes in close proximity to the membrane as well as in the membrane space.

Therefore, the observed proximity of C_{60} aggregates to lipid membranes prompted investigation of the role of nano-lipid interactions. Using thermodynamically-driven atomistic models of an idealized lipid bilayer and confirmed by NMR analysis, the potential for passive diffusion as a major contributor to cellular C_{60} loads was examined.

Molecular dynamics (MD) simulations were utilized to gain insights on the interactions of a cellular membrane with nanoparticles. A fully hydrated symmetric lipid bilayer of 1-palmitoyl-2-oleoyl-*sn*-glycero-3-phosphocholine (POPC) in the presence of a single C_{60} as well as agglomerates of C_{60} molecules was analyzed. The interactions between a single C_{60} molecule and the membrane were evaluated by computing the free energy (FE) as a function of the projection on the bilayer normal of the distance between the C_{60} molecule and the center of the bilayer. Fig. 4 reports the reconstructed FE profile of the permeation of a single C_{60} in the POPC bilayer. C_{60} is readily absorbed into the hydrophobic part of the lipid bilayer with a marked increase in the stability of the system (approximately 30 kcal mol^{-1}) and with minimal disruption of the hydrophobic environment. The preferred location (minimum of the FE profile) does not correspond to the center of the bilayer, but is shifted from the central plane towards the lipids headgroups by $0.4\text{--}0.6 \text{ nm}$. This distance corresponds to the position of the 9th and 10th carbon of the saturated alkyl chains of POPC, as shown by plotting the equilibrium distribution of the atoms' distance from the bilayer middle plane

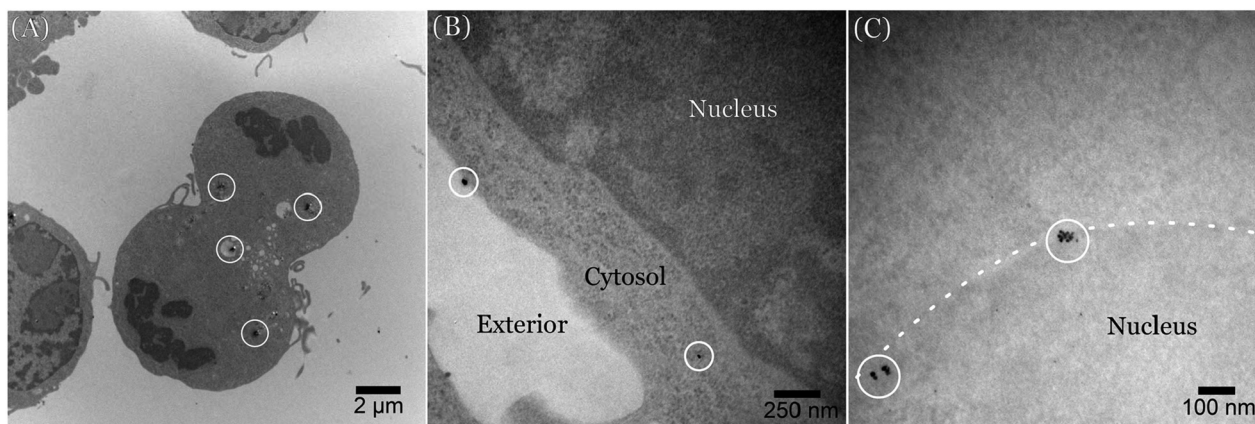


Fig. 2 No contrast transmission electron micrograph of RAW 264.7 immortalized macrophages containing terbium-endohedral C_{60} . (A) High contrast clusters of C_{60} (inside with circles) are observed in membrane-bound structures and scattered "free" throughout the cytoplasm. (B) Higher power no contrast TEM shows two major clusters of Tb@C_{60} adjacent to the cell membrane (upper left) and not bounded by lipid membrane in the cytosol. (C) High power examination of the nuclear envelope (dotted line) reveals membrane-associated clusters that are not contained in classical phagocytotic structures.



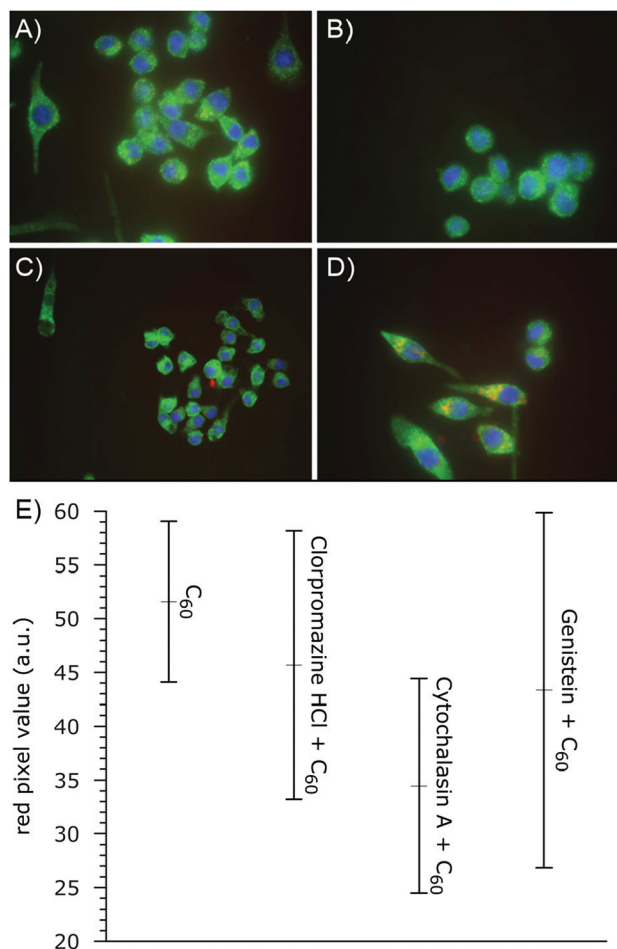


Fig. 3 Epifluorescent images of immortalized RAW 264.7 macrophages showing lack of role for endocytosis in cellular accumulation of C₆₀. (A) Baseline uptake was established following 3 h exposures to C₆₀, and a monoclonal antibody (red) was used to detect and quantify uptake. The effect of classical inhibitors of active membrane-mediated processes for cell entry was determined in the presence of (B) chlorpromazine (clathrin-mediated endocytosis), (C) cytochalasin A (F-actin polymerization) or (D) genistein (caveolin-mediated endocytosis, macropinocytosis and phagocytosis). (E) Statistical analysis of images supports diffusion rather than endo-/phagocytosis as the major route by which small clusters of C₆₀ enter the cell membrane and cytoplasm. The apparent lack of statistically significant diminution in the uptake of C₆₀ induced by the pharmacologic inhibition of clathrin/caveolin-mediated endocytosis suggests that a significant quantity of material enters the cell through other mechanisms.

(Fig. 5). The results indicate the permeation process is thermodynamically favored and barrierless.

To highlight the differences in interactions between the lipid bilayer with a single or a small cluster of C₆₀ fullerenes, we monitored the properties of a POPC membrane when a cluster of eight fullerenes (approximately 3 nm in diameter) is present in the hydrophobic region. The cluster markedly perturbed not only the acyl chains structure and organization, but also the disposition of the headgroups, causing a localized bulging of the bilayer (Fig. 6). This perturbation affects the entire lipid molecules, but is particularly marked in the region

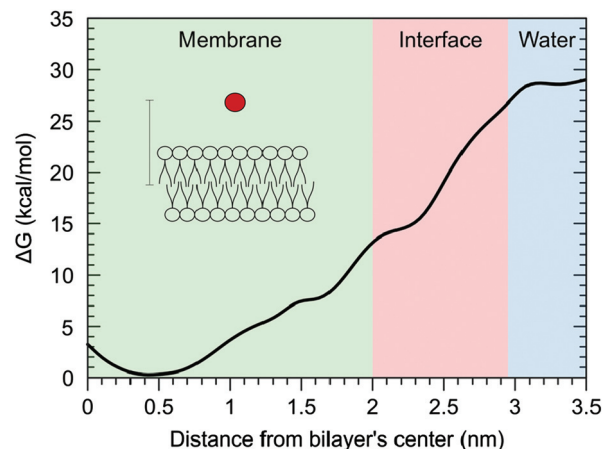


Fig. 4 Free energy profile of the permeation of a C₆₀ fullerene into a POPC bilayer as function of the distance on the membrane normal between the fullerene and the bilayer center.

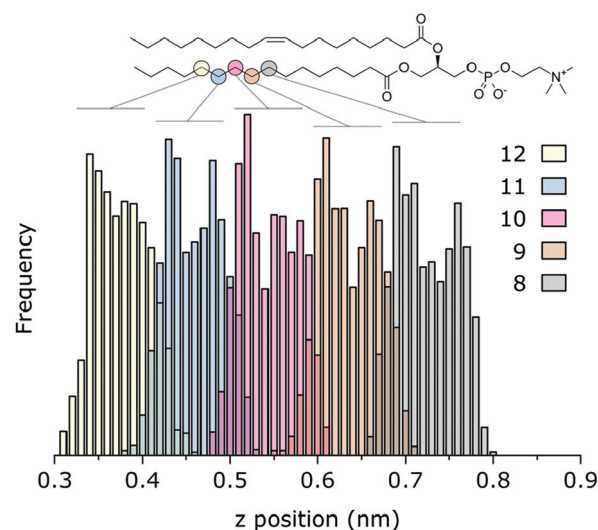


Fig. 5 Distribution of selected carbon atoms of the saturated chain of POPC. Shown as function of the distance on the bilayer normal. Zero corresponds to the center of the bilayer.

that extends from the center of the bilayer to the 9th carbon (about 0.7 nm).

Due to favorable interaction however, fullerene clusters may be short lived in the hydrophobic region of the membrane. Since the dissolution of the C₆₀ clusters could be thermodynamically favored, but slow (relatively to the simulation scale) and therefore hard to observe with an unbiased MD, we employed biased MD to study the behavior of the system during the disaggregation of the C₆₀ cluster in the membrane. Namely, we explored the changes associated with a change of the cluster radius of gyration. With this approach we are able to overcome both energetic and kinetic barriers that may affect the solubility of C₆₀ fullerenes. The results



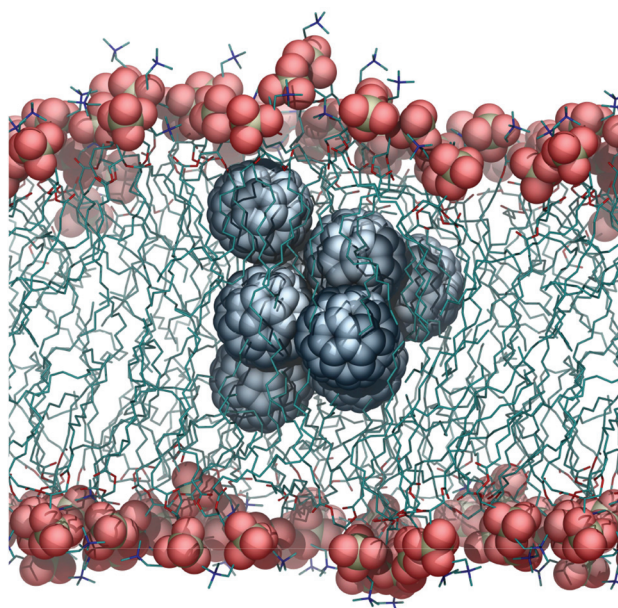


Fig. 6 Small cluster of C_{60} fullerenes in a POPC lipid bilayer.

show however, that the aggregates are not a metastable state, and disaggregation of the clusters is an extremely unlikely process. As an indicator of adhesion energy, the free-energy profile (Fig. 7) shows a clear well around the equilibrium radius (0.915 nm). The energy increases rapidly for small values of the radius of gyration (<0.9 nm), in agreement with the low compressibility of the cluster; at higher values (about 1.01 nm, which corresponds to approximately 23 kcal mol⁻¹) we observe a clear change in slope, which corresponds to the detachment of a single C_{60} from the cluster. In all cases we see the preferential disaggregation of a C_{60} situated near the

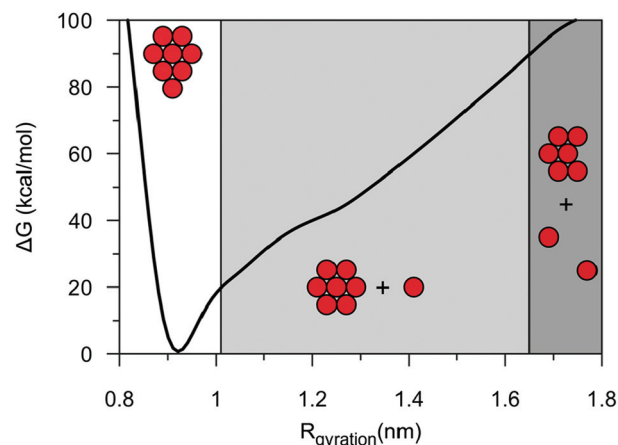


Fig. 7 Free energy profile of fullerenes with various radii of gyration in a POPC bilayer. A clear well is identified around the equilibrium radius of 0.915 nm. Energy increases rapidly at smaller radii values and shows a change in slope at higher values, corresponding to detachment of a single C_{60} .

center of the bilayer, likely due to the lower density of that region. At even higher values (approximately 1.85 nm), we observed the detachment of a second C_{60} , but this process requires very high energy (about 90 kcal mol⁻¹), making it an extremely unlikely event. Because the detachment of even one or two C_{60} molecules is a very unfavorable event (23 and 90 kcal mol⁻¹, respectively), the disaggregation of a small cluster of C_{60} in the membrane is a very unlikely occurrence. In conclusion, MD simulations show that particles readily diffuse into biological membranes. A single fullerene causes limited perturbation of the membrane, but clusters of C_{60} determine bulging and deformation of the membrane. To further analyze the interactions between nanoparticles and lipid bilayers, nuclear magnetic resonance experiments were conducted on vesicles of POPC containing C_{60} .

Deuterium and phosphorous NMR spectra were recorded to determine the influence of C_{60} on the bulk phase behavior of the POPC bilayers irrespective of the location of the C_{60} within the bilayer as well as their influence on the local structure and dynamics. To assess how C_{60} perturbs the phase behavior of the lipids⁴⁸ and assess how its presence alters the structure and dynamics^{49–53} of the lipid headgroup we have undertaken a ³¹P NMR study of C_{60} in lipid vesicles composed of d₃₁-POPC vesicles. The ³¹P spectra of POPC in absence of C_{60} is shown in Fig. 8A and is consistent with previous studies, with an axially symmetric powder pattern characterized by a chemical shielding anisotropy of approximately -30 ppm. The spectrum is typical for POPC in a liquid crystalline bilayer phase. Because

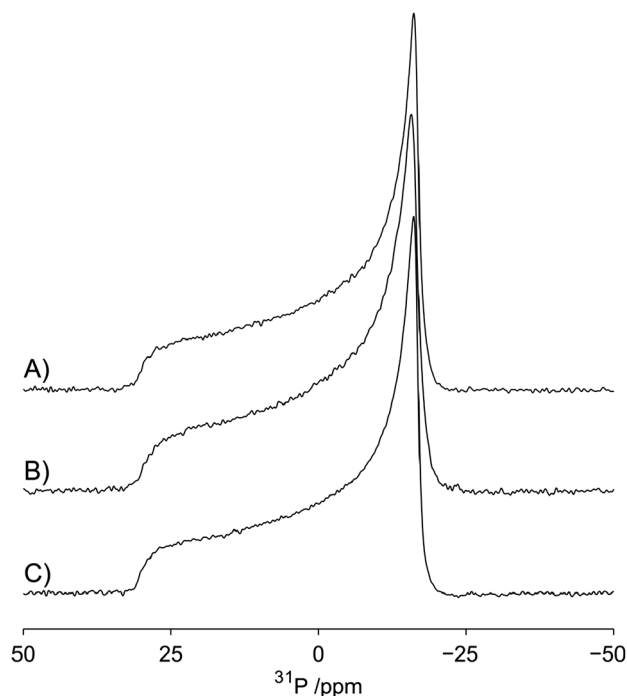


Fig. 8 Phosphorous spectra of POPC vesicles by NMR. Prepared in the presence of fullerenes, (A) at 0 μg mL⁻¹, (B) 10 μg mL⁻¹, (C) and 100 μg mL⁻¹. Data acquired at 20 °C.



the addition of C_{60} to a concentration of $10 \mu\text{g mL}^{-1}$ (Fig. 8B) does not cause any significant changes to the ^{31}P spectrum of the POPC, we conclude that at these concentrations the C_{60} has little effect on the structural (geometric) and dynamics properties of the headgroups of the bilayer. The ^{31}P spectra of POPC for increased concentration of C_{60} ($100 \mu\text{g mL}^{-1}$) are reported in Fig. 8C and show a small reduction in the chemical shielding anisotropy, as evidenced by the $\pi/2$ edge of the powder pattern shifting from -16.18 to -15.77 ppm. Such a reduction in ^{31}P chemical shielding anisotropy is consistent with small changes in lipid headgroup geometry or dynamics, or both.^{49–53} Our results therefore, reveal a slight perturbation in head position (geometry) and dynamics at high concentrations. In contrast to studies of surface-modified fullerenes, such as fullerlenols, at the concentrations studied, we see no evidence for the disruption of the bilayer such as has been observed for other bilayer systems.⁵⁴

Furthermore, the observed changes in the distribution of intensity in the ^{31}P spectrum reflect differences in the orientational distribution of the lipids within the sample^{48,55–57} with an increase in intensity in the low-field region corresponding to an enhanced probability of lipids aligning with their long axis parallel to the magnetic field. On the contrary, typical static ^{31}P NMR spectra of lipid vesicles exhibit a reduced intensity in the low-field region due to the preferred orientation of lipids with their long axes perpendicular to the applied magnetic field, arising from their intrinsic diamagnetic anisotropy. This observation indicates that at concentration of $100 \mu\text{g mL}^{-1}$ the C_{60} enhances the rigidity of the membrane reducing its ability to deform, in this case in response to the applied magnetic field.

The ^2H spectra show that the presence of C_{60} especially at a concentration of $100 \mu\text{g mL}^{-1}$ also results in an increase in chain mobility, as indicated by the reduction in the width of the quadrupolar splittings and by the order parameter, S_{CD} . The order parameter profiles (Fig. 9) obtained for the d_{31} -POPC bilayer in presence of 0, 10 and $100 \mu\text{g mL}^{-1}$ of C_{60} , reveal a small but reproducible concentration-dependent reduction in order parameter. In absence of C_{60} , the observed behavior is consistent with previous research, specifically the order parameter decreases along the length of the acyl chain, indicative of the increased mobility typically found within the center of the lipid bilayer.²⁴ At the lowest C_{60} concentration ($10 \mu\text{g mL}^{-1}$) the reduction is mostly observed at the 9th and 10th position in the chain. At the highest concentration of C_{60} ($100 \mu\text{g mL}^{-1}$) a larger reduction in order parameter is observed from the 8th carbon to the methyl end of the acyl chain. Thus, with increasing C_{60} concentrations, the *sn*-1 chains become on average more mobile (Fig. 9). This is consistent with C_{60} increasing the disorder and mobility towards the center of the lipid bilayer.

The agreement between NMR data and simulations suggests that at the lower concentration, the C_{60} molecules tend to enter the lipid bilayer individually, or possibly as a pair, causing only a limited alteration in the position of aliphatic chains and no changes in the headgroups position. At

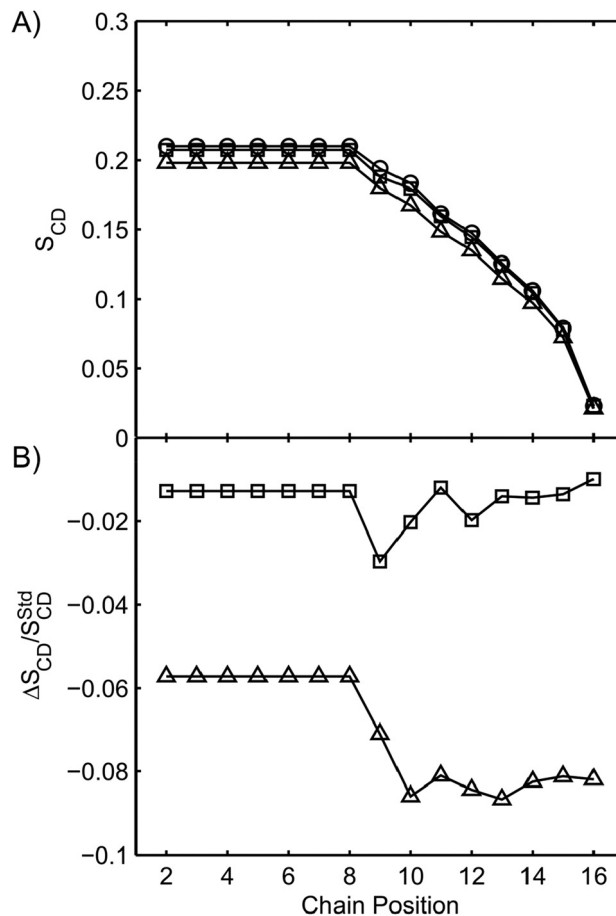


Fig. 9 (A) Order parameter profile for d_{31} -POPC prepared in the presence of fullerenes, at $0 \mu\text{g mL}^{-1}$ (circle), $10 \mu\text{g mL}^{-1}$ (square), and $100 \mu\text{g mL}^{-1}$ C_{60} (triangle). (B) Perturbation in order parameter with respect to vesicles in absence of C_{60} . Data acquired at 20°C .

higher concentration of C_{60} , the agreement between the observed S_{CD} plot and the perturbation of the bilayer computed with MD (Fig. 6) suggests the presence of aggregates inside the bilayer.

As a consequence of the induced disorder in the lipid chain as function of the concentrations of nanoparticles, we hypothesized a shift in the phase transition temperature toward lower values. This hypothesis was explored with deuterium NMR studies at different temperatures (Fig. 10). As the temperature increases, we see a progressive reduction in 1st moment that represents the weighted average deuterium splitting; it provides a convenient unit with which to parameterize the width of the spectra and has been extensively used to characterize lipid phase transitions.²² At -5°C a rapid reduction (occurring in less than 3°C) in the 1st moment is observed in POPC bilayers in the absence of the fullerene C_{60} . This rapid reduction arises from the increased chain mobility associated with the cooperative disordering of the lipid chains as the lipids pass through the phase transition between the gel and liquid crystalline phases. The phase transition temperature is similar to previously reported values for d_{31} -POPC.²⁴



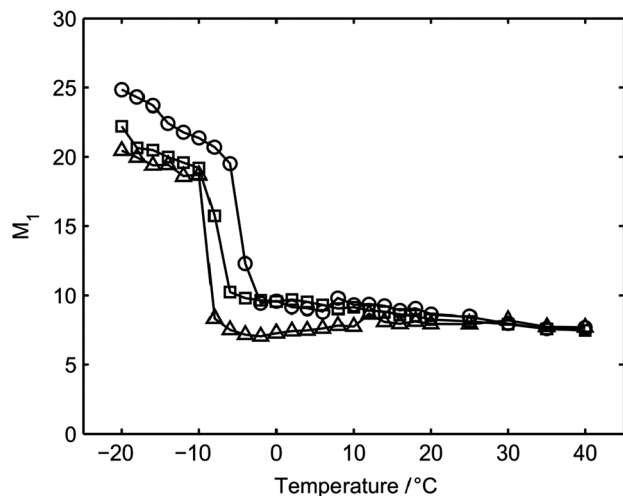


Fig. 10 Temperature dependence of the first moment of deuterium NMR spectra recorded from d_{31} -POPC in the presence of $0 \mu\text{g mL}^{-1}$ (circle), $10 \mu\text{g mL}^{-1}$ (square) and $100 \mu\text{g mL}^{-1}$ C_{60} (triangle).

Above this temperature, the 1st moment continues to progressively decline as the temperature increases. The addition of the fullerene C_{60} to the bilayers at concentrations of $10 \mu\text{g mL}^{-1}$ and $100 \mu\text{g mL}^{-1}$ results in a reduction in the phase transition to $-8 \text{ }^{\circ}\text{C}$ and $-9 \text{ }^{\circ}\text{C}$, respectively, indicative of the C_{60} disrupting the stability of the gel phase. Within the accuracy of the measurements, the temperature range over which the phase transition occurs appears insensitive to the concentration, spanning $3\text{--}4 \text{ }^{\circ}\text{C}$ in each case, suggesting that the presence of the C_{60} within the sample has no effect on the cooperative nature of the phase transition. Both above and below the phase transition, the presence of the fullerene C_{60} within the sample leads to enhanced mobility within the acyl chains as characterized by a lower 1st moment for a given temperature, consistently with our initial hypothesis.

Conclusions

The aim of this study was to determine the mechanisms of uptake of C_{60} fullerenes into compartments of living cells, by using a combination of classical biological, biophysical and computational techniques. Modes of entry studied were endocytosis/pinocytosis and passive permeation of cellular membranes. Cultures of RAW 264.7 immortalized murine macrophage were used as model for immune-competent cells. These cells are well suited to endo-/phagocytosis. Terbium-endohedral C_{60} fullerenes were employed to provide identification of individual and clusters of nanoparticles *in situ*. Using transmission electron microscopy, particles were observed in association with or in cell/nuclear membranes as well as unbound by biological membranes in the cytoplasm of immortalized macrophages. Although the cell type chosen for this study is well suited to endo-/phagocytosis, our experiments

could not find evidence for a major contribution by this mode of entry.

Since particles were observed in and close to lipid bilayers *in vitro*, we further analyzed the interactions between nanoparticles and lipid bilayers using molecular dynamics simulations. Computational modeling of C_{60} interacting with a POPC lipid bilayers, representative of the cellular membrane, show that particles readily diffuse into biological membranes and find a thermodynamically stable equilibrium in an eccentric position within the bilayer. At low concentrations, fullerenes enter the membrane individually and cause limited perturbation; however, at higher concentrations the clusters in the membrane causes deformation of the membrane.

These findings are further supported by NMR experiments of model membranes that reveal deformation of the cell membrane, confirming distortions in membrane morphology that are consistent with the results of atomistic models. However, neither the model nor NMR experiments are able to explain the mechanism of release from lipid bilayers that result in the presence of unbounded particles in the cytoplasm.

Future studies should be aimed at atomistic and molecular mechanisms that take into account integral proteins, the glyco-calyx and other complexities found in living cells. It is also important to note that higher concentrations of C_{60} are required for detection of nanomaterial in nmr studies. One possible confounder might be that accumulation in biological membranes may only occur after saturation of other cellular depots. Additional studies are required to determine whether or not *prima facie* accumulation of C_{60} in the intramembrane space is of primary biological importance.

This study is the first of its kind that suggests a marginal role for endo-/phagocytosis in the cellular uptake of C_{60} . We present new evidence of a major contributor to cellular particle loads through the passive entry and integration of C_{60} particles into biological membranes. NMR and electron microscopy confirms the ability of C_{60} to enter and distort membrane morphology their presence in unbound clusters throughout the cell. Moreover, though incomplete, the results of this study provide a plausible mechanism by which particles may integrate into membranes and later escape through as yet unidentified pathways. The biological significance of these findings remains to be determined.

Acknowledgements

Research reported in this publication was supported by the National Institute of Environmental Health Sciences of the National Institutes of Health under Award Number T32ES007062 (KAR), ES R01 088546 (MAP). The content is solely the responsibility of the authors and does not necessarily represent the official views of the National Institutes of Health. Partial support was also provided by U.S. DOE BES Grant no. DE-SC0002619 (PE and AV).



MAP and KAR thank Tessa Adzemovic and Jennifer Fernandez for their technical assistance.

References

- 1 K. Aschberger, H. J. Johnston, V. Stone, R. J. Aitken, C. L. Tran, S. M. Hankin, S. A. K. Peters and F. M. Christensen, *Regul. Toxicol. Pharmacol.*, 2010, **58**, 455–473.
- 2 G. D. Nielsen, M. Roursgaard, K. A. Jensen, S. S. Poulsen and S. T. Larsen, *Basic Clin. Pharmacol. Toxicol.*, 2008, **103**, 197–208.
- 3 H. J. Johnston, G. R. Hutchison, F. M. Christensen, K. Aschberger and V. Stone, *Toxicol. Sci.*, 2010, **114**, 162–182.
- 4 T. Y. Zakharian, A. Seryshev, B. Sitharaman, B. E. Gilbert, V. Knight and L. J. Wilson, *J. Am. Chem. Soc.*, 2005, **127**, 12508–12509.
- 5 A. Montellano, T. D. Ros, A. Bianco and M. Prato, *Nanoscale*, 2011, **3**, 4035–4041.
- 6 R. Chang and A. Violi, *J. Phys. Chem. B*, 2006, **110**, 5073–5083.
- 7 G. Oberdörster, E. Oberdörster and J. Oberdörster, *Environ. Health Perspect.*, 2005, **113**, 823–839.
- 8 A. Verma and F. Stellacci, *Small*, 2010, **6**, 12–21.
- 9 S. Bosi, T. Da Ros, G. Spalluto and M. Prato, *Eur. J. Med. Chem.*, 2003, **38**, 913–923.
- 10 Z. Markovic, B. Todorovic-Markovic, D. Kleut, N. Nikolic, S. Vranjes-Djuric, M. Misirkic, L. Vucicevic, K. Janjetovic, A. Isakovic, L. Harhaji, B. Babic-Stojic, M. Dramicanin and V. Trajkovic, *Biomaterials*, 2007, **28**, 5437–5448.
- 11 S. Deguchi, R. G. Alargova and K. Tsujii, *Langmuir*, 2001, **17**, 6013–6017.
- 12 P. Spohn, C. Hirsch, F. Hasler, A. Bruinink, H. F. Krug and P. Wick, *Environ. Pollut.*, 2009, **157**, 1134–1139.
- 13 B. Zhang, M. Cho, J. D. Fortner, J. Lee, C.-H. Huang, J. B. Hughes and J.-H. Kim, *Environ. Sci. Technol.*, 2009, **43**, 108–113.
- 14 T. dos Santos, J. Varela, I. Lynch, A. Salvati and K. A. Dawson, *PLoS One*, 2011, **6**, e24438.
- 15 I. R. Nabi and P. U. Le, *J. Cell Biol.*, 2003, **161**, 673–677.
- 16 M. Bohdanowicz and S. Grinstein, *Physiol. Rev.*, 2013, **93**, 69–106.
- 17 S. Braun, H.-O. Kalinowski and S. Berger, *150 and more basic NMR experiments: a practical course*, Wiley-VCH, Weinheim, 1998, 2, expanded ed.
- 18 J. D. van Beek, *J. Magn. Reson.*, 2007, **187**, 19–26.
- 19 M. A. McCabe and S. R. Wassail, *Solid State Nucl. Magn. Reson.*, 1997, **10**, 53–61.
- 20 J. H. Davis, *Biochim. Biophys. Acta, Rev. Biomembr.*, 1983, **737**, 117–171.
- 21 A. Salmon, S. W. Dodd, G. D. Williams, J. M. Beach and M. F. Brown, *J. Am. Chem. Soc.*, 1987, **109**, 2600–2609.
- 22 J. H. Davis, *Biophys. J.*, 1979, **27**, 339–358.
- 23 L. J. Burnett and B. H. Muller, *J. Chem. Phys.*, 1971, **55**, 5829–5831.
- 24 J. Seelig and A. Seelig, *Q. Rev. Biophys.*, 1980, **13**, 19–61.
- 25 F. A. Nezil and M. Bloom, *Biophys. J.*, 1992, **61**, 1176–1183.
- 26 C. P. Slichter, *Principles of Magnetic Resonance*, Springer, Berlin Heidelberg, Berlin, Heidelberg, 1990, vol. 1.
- 27 J. C. Phillips, R. Braun, W. Wang, J. Gumbart, E. Tajkhorshid, E. Villa, C. Chipot, R. D. Skeel, L. Kalé and K. Schulten, *J. Comput. Chem.*, 2005, **26**, 1781–1802.
- 28 M. Bonomi, D. Branduardi, G. Bussi, C. Camilloni, D. Provasi, P. Raiteri, D. Donadio, F. Marinelli, F. Pietrucci, R. A. Broglia and M. Parrinello, *Comput. Phys. Commun.*, 2009, **180**, 1961–1972.
- 29 J. B. Klauda, R. M. Venable, J. A. Freites, J. W. O'Connor, D. J. Tobias, C. Mondragon-Ramirez, I. Vorobyov, A. D. MacKerell and R. W. Pastor, *J. Phys. Chem. B*, 2010, **114**, 7830–7843.
- 30 K. Vanommeslaeghe, E. Hatcher, C. Acharya, S. Kundu, S. Zhong, J. Shim, E. Darian, O. Guvench, P. Lopes, I. Vorobyov and A. D. Mackerell Jr., *J. Comput. Chem.*, 2010, **31**, 671–690.
- 31 D. J. Price and C. L. Brooks, *J. Chem. Phys.*, 2004, **121**, 10096.
- 32 T. Darden, D. York and L. Pedersen, *J. Chem. Phys.*, 1993, **98**, 10089–10092.
- 33 A. T. Brünger, *X-PLOR: Version 3.1: a System for X-ray Crystallography and NMR*, Yale University Press, 1992.
- 34 J.-P. Ryckaert, G. Ciccotti and H. J. C. Berendsen, *J. Comput. Phys.*, 1977, **23**, 327–341.
- 35 S. E. Feller, Y. Zhang, R. W. Pastor and B. R. Brooks, *J. Chem. Phys.*, 1995, **103**, 4613–4621.
- 36 G. J. Martyna, D. J. Tobias and M. L. Klein, *J. Chem. Phys.*, 1994, **101**, 4177–4189.
- 37 A. Barducci, G. Bussi and M. Parrinello, *Phys. Rev. Lett.*, 2008, **100**, 020603.
- 38 S. Jo, T. Kim, V. G. Iyer and W. Im, *J. Comput. Chem.*, 2008, **29**, 1859–1865.
- 39 Y.-H. Luo, L. W. Chang, P. Lin, Y.-H. Luo, L. W. Chang and P. Lin, *BioMed Res. Int.*, 2015, **2015**, e143720.
- 40 M. A. Dobrovolskaia, P. Aggarwal, J. B. Hall and S. E. McNeil, *Mol. Pharm.*, 2008, **5**, 487–495.
- 41 C. D. Walkey, J. B. Olsen, H. Guo, A. Emili and W. C. W. Chan, *J. Am. Chem. Soc.*, 2012, **134**, 2139–2147.
- 42 J. Brant, H. Lecoanet, M. Hotze and M. Wiesner, *Environ. Sci. Technol.*, 2005, **39**, 6343–6351.
- 43 H. Hyung and J.-H. Kim, *Water Res.*, 2009, **43**, 2463–2470.
- 44 V. L. Colvin, *Nat. Biotechnol.*, 2003, **21**, 1166–1170.
- 45 M. Marsh and H. T. McMahon, *Science*, 1999, **285**, 215–220.
- 46 R. G. Parton and K. Simons, *Nat. Rev. Mol. Cell Biol.*, 2007, **8**, 185–194.
- 47 P. Sens and M. S. Turner, *Biophys. J.*, 2004, **86**, 2049–2057.
- 48 J. Seelig, *Biochim. Biophys. Acta, Biomembr.*, 1978, **515**, 105–140.
- 49 J. Seelig, *Q. Rev. Biophys.*, 1977, **10**, 353–418.
- 50 F. Lindström, P. T. F. Williamson and G. Gröbner, *J. Am. Chem. Soc.*, 2005, **127**, 6610–6616.



- 51 D. J. Semchyschyn and P. M. Macdonald, *Magn. Reson. Chem.*, 2004, **42**, 89–104.
- 52 B. Bechinger and J. Seelig, *Biol. Chem. Hoppe-Seyler*, 1990, **371**, 758–758.
- 53 J. P. F. Doux, B. A. Hall and J. A. Killian, *Biophys. J.*, 2012, **103**, 1245–1253.
- 54 P. P. Brisebois, A. A. Arnold, Y. M. Chabre, R. Roy and I. Marcotte, *Eur. Biophys. J.*, 2012, **41**, 535–544.
- 55 T. Pott and E. J. Dufourc, *Biophys. J.*, 1995, **68**, 965–977.
- 56 F. Picard, M.-J. Paquet, J. Levesque, A. Bélanger and M. Auger, *Biophys. J.*, 1999, **77**, 888–902.
- 57 E. L. Ashworth Briggs, R. G. B. Gomes, M. Elhussein, W. Collier, I. Stuart Findlow, S. Khalid, C. J. McCormick and P. T. F. Williamson, *Biochim. Biophys. Acta, Biomembr.*, 2015, **1848**, 1671–1677.

